Electronic Supplementary Information

Extremely strengthening fatigue resistance, elastic restorability and thermodynamic stability of soft transparent self-healing network based on dynamic molecular confinement-induced bioinspired nanostructure

Tong Liu,[a,b] ChuanLong Li,[c] Hai Yao,[a] FuYao Sun,[a] Lin Wang,[a] BoWen Yao,[a] JianHua Xu*[a,b,d] and JiaJun Fu*[a]

[a]School of Chemistry and Chemical Engineering, Nanjing University of Science and Technology, Nanjing 210094, China.
[b]Joint Laboratory of Advanced Biomedical Materials (NFU-UGent), College of Chemical Engineering, Nanjing Forestry University, Nanjing 210037, China.
[c]College of Polymer Science and Engineering, State Key Laboratory of Polymer Materials and Engineering, Sichuan University, Chengdu 610065, China.
[d]State Key Laboratory of Coordination Chemistry, Nanjing University, Nanjing 210093, China.

***Corresponding authors: JianHua Xu, email: xujianhua931118@163.com and JiaJun Fu, fujiajun668@gmail.com**

General characterizations

The ^{1}H NMR spectra were captured using a Bruker AVANCE III 500 MHz spectrometer in room temperature with dimethyl sulfoxide-d6 as solvent. FTIR spectra were recorded using a Bruker Tensor II spectrometer equipped with a Specac Golden Gate MK II ATR in the range of 4000 cm^{-1} to 600 cm^{-1}. UV-vis transmittance spectra were recorded using a Thermal Fisher E220 spectrophotometer. DSC analysis was conducted using a DSC-25 (TA instruments) and the temperature range was from 0 °C to 150 °C with a heating/cooling rate of 10 °C min^{-1} in a nitrogen atmosphere. X-ray photoelectron spectroscopy (XPS) was performed on a PHI Quantera II X-ray photoelectron spectrometer using focused Al Kα radiation (15 kV). Bruker Multimode 8 was used to capture AFM images in tapping mode. SEM images were acquired with a FEI Quanta 250FEG field emission electron microscope. TGA measurement was conducted on a Mettler 851e in nitrogen atmosphere from 50 to 800 °C with a heating rate of 20 °C min^{-1}. The Signals of resistance change for cyclic extension-release test and human activity was measured by a Keithley 2450 SourceMeter combined with mechanical testing instrument. SAXS measurements were done on a Bruker NanoSTAR. Optical microscopy images were recorded using a Jiangnan MV3000 optical microscope. The GPC analysis was performed in THF using PolyPore columns (Agilent), which were connected in series with a DAWN multiangle laser light scattering (MALLS) detector and an Optilab TrEX differential refractometer, both of which were provided by Wyatt Technology. The sheet resistances were determined using the RTS-9 4-point probes resistivity measurement system, which was manufactured by 4 PROBES TECH.

Mechanical characterization

The tensile tests, fracture tests and fatigue tests were conducted on universal testing machine (Shimadzu AGS-X). The dimensions of all the rectangular samples were 20 × 5 × 1 mm^3. All Mechanical test were performed at a rate of 100 mm min^{-1}. Three samples were tested to obtain the mean values of Young's modulus, strength and strain. The fracture tests were determined using the single-edge notch test. Before fracture tests, the middle of the rectangle splines needed to be pre-cut with 1 mm notch in the direction of the width. The fracture toughness (G_c) was calculated from corrected Green-smith formula:

$$G_c = \frac{6Wc}{\sqrt{\lambda_c}}$$

where c is the notch length; W is the strain energy calculated by integration of the stress-strain curve of an un-notched specimen until λ_c; λ_c is the strain at break of notched specimen.

For fatigue tests, a side of the specimen needed to be pre-cut by 1 mm. Then, the fatigue tests were performed on pre-notched specimens with a span of 10 mm under cyclic tensile test at a rate of 100 mm min^{-1}. The applied energy release rate *G* was calculated as the following formula：

$$W(\lambda_{max}, N) = \int_{1}^{\lambda_{max}} S d\lambda$$

$$G(\lambda^A, N) = 2k(\lambda^A) \cdot C(N) \cdot W(\lambda^A, N)$$

where k is a varying function of the applied stretch expressed as $k=3 \cdot \lambda_{max}^{-1/2}$; c is the crack length under N cyclic stretching; W is the strain energy density determined on the integral area of the stress-strain curve of an unnotched sample over N cycles of applied stretch λ^A after waiting for 12 h.

Self-healing testing

For self-healing test of mechanical properties, we cut the rectangular sample into two halves with a razor and spliced them together, then placed them at room temperature for healing. The specimens with different healing times were subjected to tensile tests to obtain the stress-strain curves. The healing efficiency, η, was defined as the ratio between the integral area of healed sample to that of the pristine one under stress-strain curves. At least three specimens were tested to obtain the mean value of healing efficiencies.

For repairable tests of conductivity during dynamic deformation, a 0.1 mm depth of crack was pre-cut in the surface of Ag NWs/SHPU-SNS-0.3 and repaired at room temperature. The repaired specimens were conducted to cyclic tension and the curve of resistance change was recorded.

MD simulation test

An all-atom molecular dynamics (AAMD) simulation was performed by Accelrys Material Studio 2020 with COMPASSII force field. The box was constructed using Amouphous Cells and each box contained 5 polymer chains. Every polymer chain consisted of five hard and four soft segments. For polymer in SHPU-SNS-0.3 system, there are 2 UPy chain extenders in 5 hard segments. The structures were annealed via one annealing cycle including a linear heating process from 300 K to 500 K and a linear cooling process from 500 K to 300 K. Then, the system was carried out in a 1 fs equilibration step followed by 2 ns NPT ensemble at one bar pressure. The mean square displacement (MSD), cohesive energy of hard segment was obtained from the last equilibrium system.

The cohesive energy of hard segment per chain is defined as the average energy per chain required to separate all the polymer chains in a condensed state into infinite distance from each other. In our systems, the cohesive energy of hard segment per chain was calculated by the following equation:

$$E_{cohesive} = \frac{\sum_{i=1}^{5} E_{hard}^{isolated}(i) - E_{hard}^{5}}{5}$$

where $E^{isolated}_{hard}$ is the average potential energy of hard segments in an isolated polymer chain in vacuum, E^{5}_{hard} is the average potential energy of the condensed system consisting of hard segments in five polymer chains. For SHPU-WNS system, E^{5}_{hard} = -3007.67 kcal/mol and $E^{isolated}_{hard}$ = -569.84 kcal/mol, $E_{cohesive}$ = 31.69 kcal/mol. For SHPU-SNS-0.3 system, E^{5}_{hard} = -4176.42 kcal/mol and $E^{isolated}_{hard}$ = -786.54 kcal/mol, $E_{cohesive}$ = 48.74 kcal/mol.

Mean square displacement (MSD) determines the displacement of molecules followed with time which can be described as:

$$MSD = \left\langle \left| r_i(t) - r_i(0) \right|^2 \right\rangle$$

where the $r_i(t)$ represents the position vector of atom at time t and $r_i(0)$ is the initial position vector.

1. Electronic Supplementary Figures

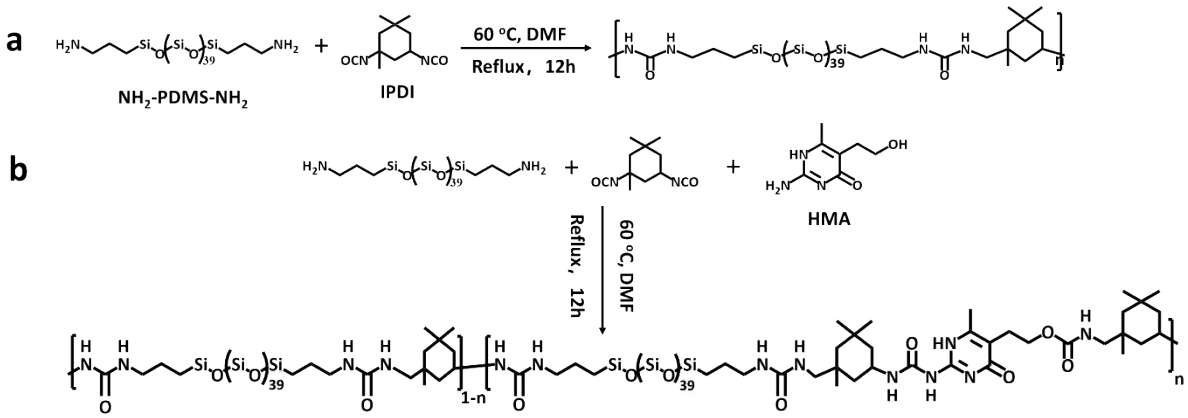

Fig. S1 Schematic illustration of the synthetic procedure of a) SHPU-WNS and b) SHPU-SNS-x. SHPU-WNS was synthesized via polycondensation reaction between NH_2-PDMS-NH_2 and IPDI, and SHPU-SNS-x were synthesized via a polycondensation reaction between NH_2-PDMS-NH_2, IPDI and HMA motifs. The detailed preparation processes were elaborated in the synthesis section of SHPU-WNS and SHPU-SNS-0.3.

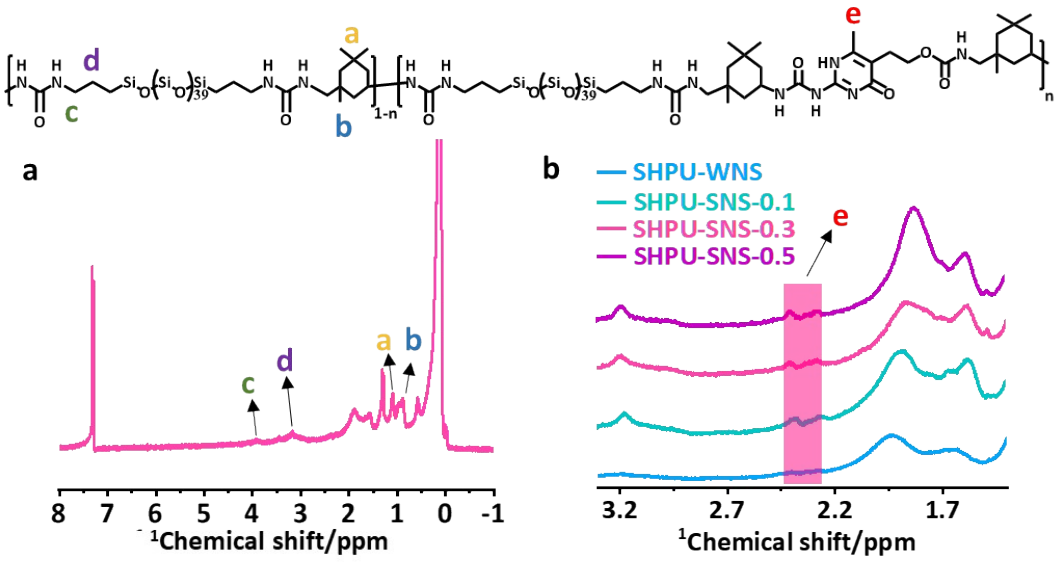

Fig. S2 a) ^{1}H NMR spectrum of SHPU-SNS-0.3. b) ^{1}H NMR spectrum of SHPU-WNS and SHPU-SNS-x from 3.3 ppm to 1.3 ppm. The ratios of signals for -CH_3 on UPy motifs confirmed that UPy motifs were successfully embedded into the polymer chains of SHPU-SNS-x.[1]

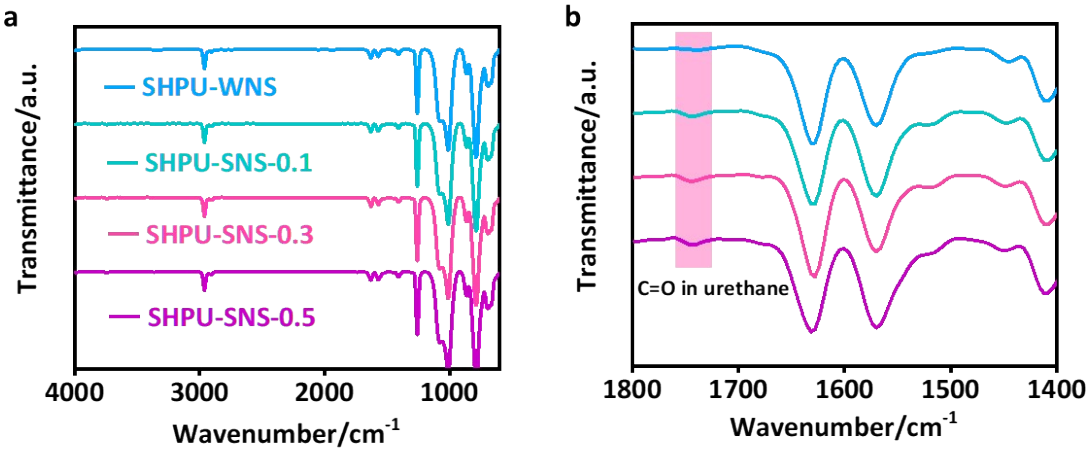

Fig. S3 FT-IR spectra of SHPU-WNS and SHPU-SNS-x. a) Full spectra in the range of 600-4000 cm^{-1}. b) Enlarged spectra from 1400-1800 cm^{-1}. With the increase of UPy motifs, the characteristic peak of -C=O in urethane increased gradually, which confirmed successful incorporation of UPy motifs.

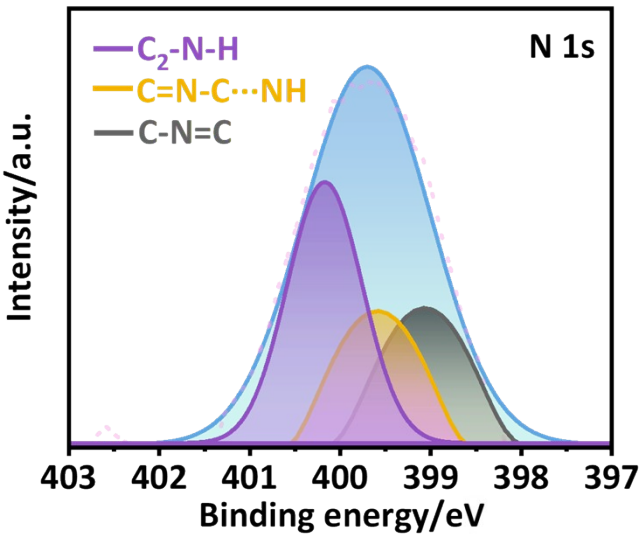

Fig. S4 N 1s spectra of SHPU-SNS-0.3. Three peaks at 399.1, 399.6, and 400.2 eV in the N 1s region of SHPU-SNS-0.3 was assigned to free -C-N=C, bonded C=N-C···NH, C_2-N-H, respectively, suggesting the existence of UPy motifs and the formation of new physical crosslinks in SHPU-SNS-0.3.

Sample	M_n (g/mol)	M_w (g/mol)	PDI (M_w/M_n)
SHPU-WNS	49135	95183	1.94
SHPU-SNS-0.1	49677	90413	1.82
SHPU-SNS-0.3	54309	103732	1.91
SHPU-SNS-0.5	56209	105673	1.88

Fig. S5 Summary of molecular weight for SHPU-WNS and SHPU-SNS-x. M_n is the number-average molecular weight; M_w is the weight-average molecular weight; PDI is the polydispersity index (M_w/M_n).

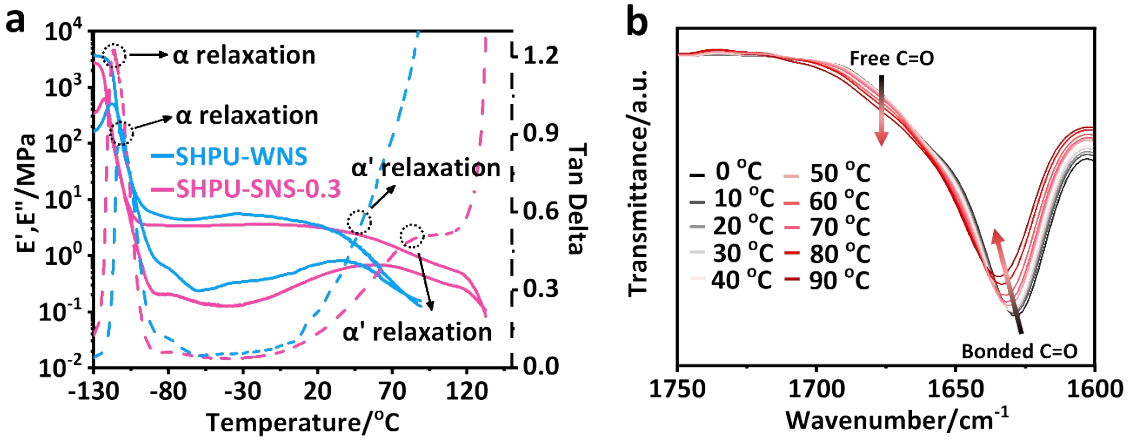

Fig S6. a) Temperature dependency of the storage modulus (E'), loss modulus (E''), and loss factor tanδ for SHPU-WNS and SHPU-SNS-0.3 from -130 to 135 °C. b) Temperature-dependent FTIR spectra of SHPU-SNS-0.3 upon heating from 0 to 90 °C. As shown in Fig. S6a, the peaks at about -110 °C were assigned to the alpha relaxations of soft PDMS chains. Besides, the peaks from 0 to 90 °C were assigned to the α′ relaxation of the dynamic hard domains, which were confirmed by temperature-dependent FTIR (Fig. S6b). Specifically, when the heating temperature increased from 0 to 90 °C, the peak of H-bonded C=O motifs gradually decreased, while the peak of free C=O motifs increased accordingly. These variations demonstrated the dissociation of ordered hydrogen bonding in the hard domains of SHPU-SNS-0.3. Therefore, the peaks from 0 to 90 °C were the α′ relaxation of hard domains assembled by abundant hydrogen bonds.

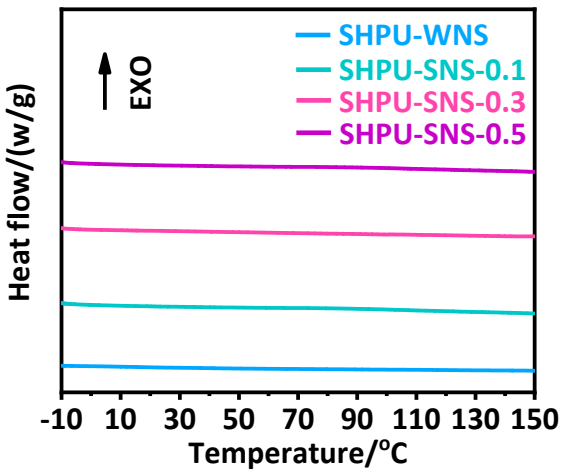

Fig. S7 DSC curves of SHPU-WNS and SHPU-SNS from -10 to 150 °C.

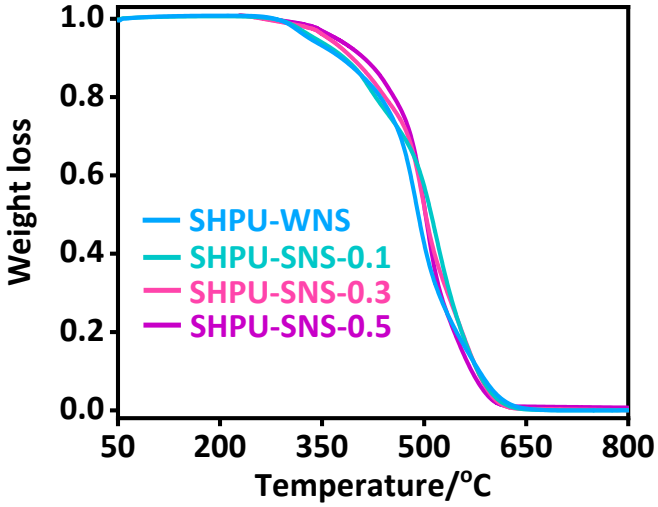

Fig. S8 TGA curves of SHPU-WNS and SHPU-SNS-x heating from 50 °C to 800 °C

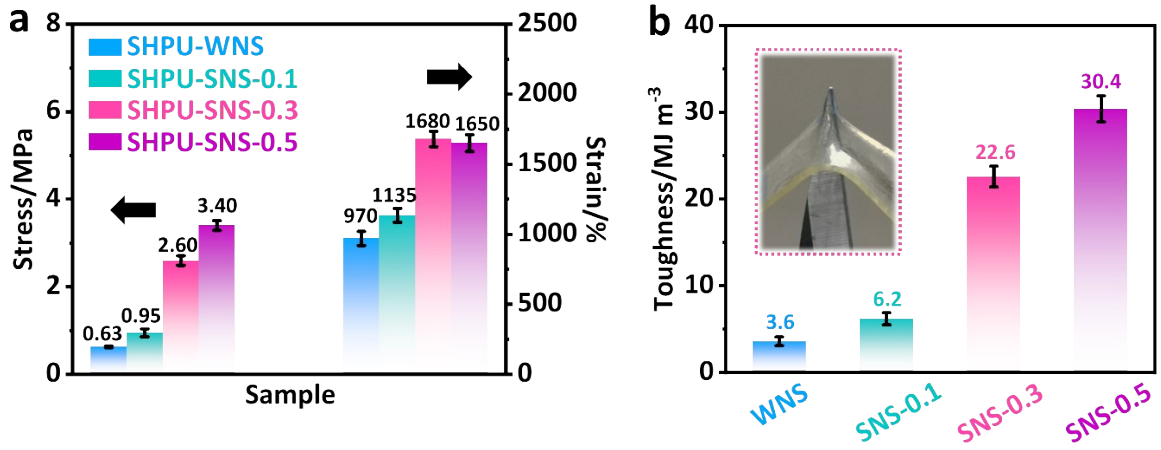

Fig. S9 a) Comparison on the stress and strain data of SHPU-WNS and SHPU-SNS-x. b) Comparison on the toughness of SHPU-WNS and SHPU-SNS-x, inserting photograph showing the high toughness of SHPU-SNS-0.3. As the UPy content increased from 10 mol% to 50 mol%, the tensile stress increased from 0.95±0.09 MPa to 3.40±0.11 MPa, the tensile strain increased from 1135%±50% to 1680%±60% and then decreased to 1650%±90%, the toughness increased from 6.2±0.7 MJ m^{-3} to 30.4±1.5 MJ m^{-3} (Fig. S9). Meanwhile, a robust yet tough SHPU-WNS-0.3 (thickness: ~1.0 mm) could successfully endure puncture from a sharp needle (Fig. S9b), which was urgently required for durable strain-devices but arduous to achieve.

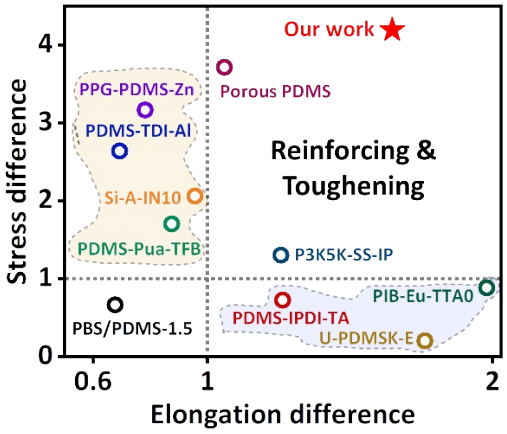

Fig. S10 The ratio of stress versus the ratio of elongation, suggesting a simultaneous increase in strength and ductility of SHPU-SNS-0.3, which was superior to the state-of-the-art soft materials. The statistical data could be found in Table S2.

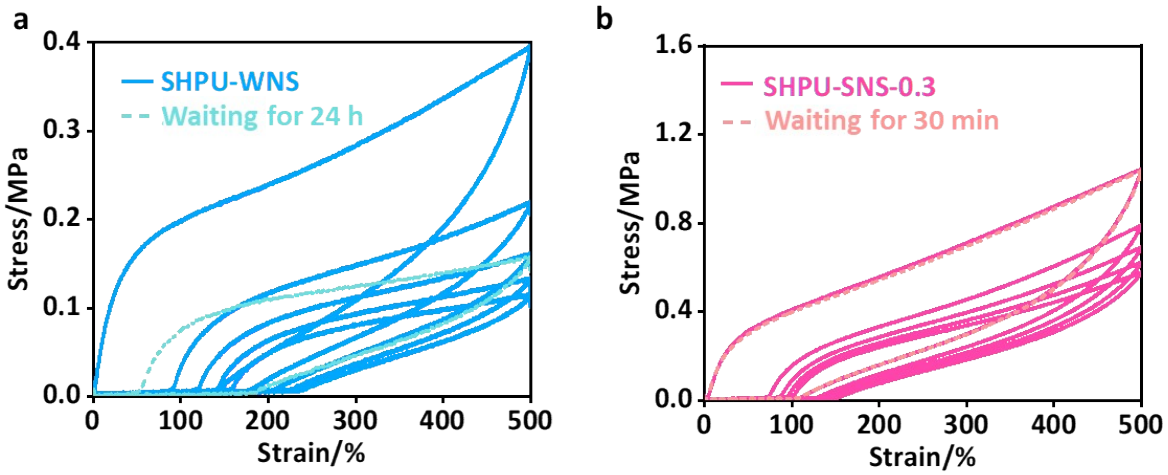

Fig. S11 Consecutive cyclic loading curves of a) SHPU-WNS and b) SHPU-SNS-0.3 at 500% strain without delay and the corresponding recovered curve after relaxation. After five successive cycles of loading-unloading and then relaxation for 30 min, the hysteresis loop and residual strain of SHPU-SNS-0.3 could be completely recovered. In sharp contrast, SHPU-SNS failed to shrink back to its initial length with a pronounced residual strain even after 24 h relaxation.

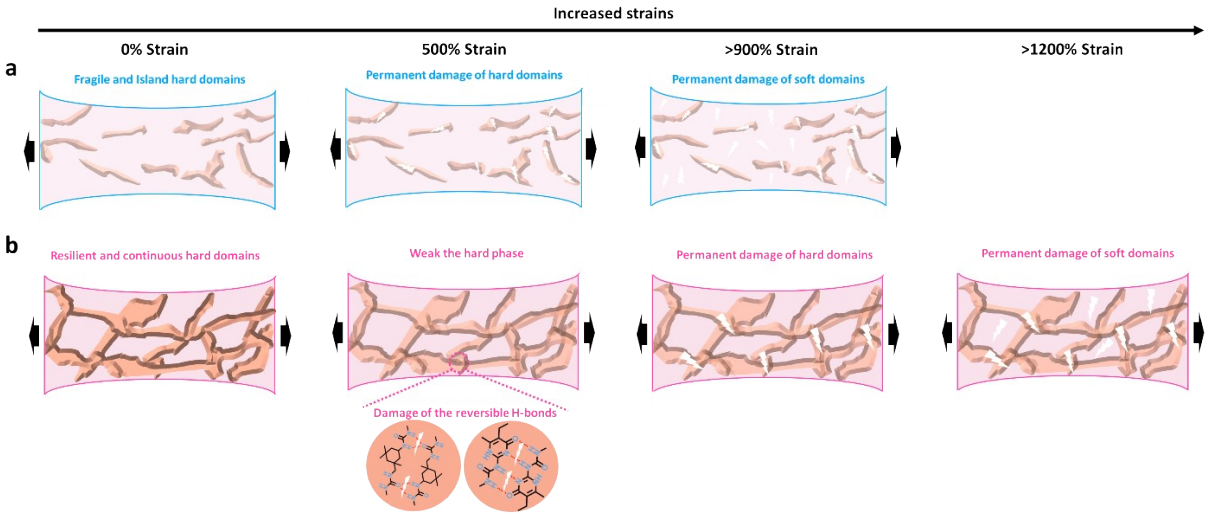

Fig. S12 Illustration of the evolution in cross-linkers and nanophase structures of a) SHPU-WNS and b) SHPU-SNS-0.3 under different applied strains.

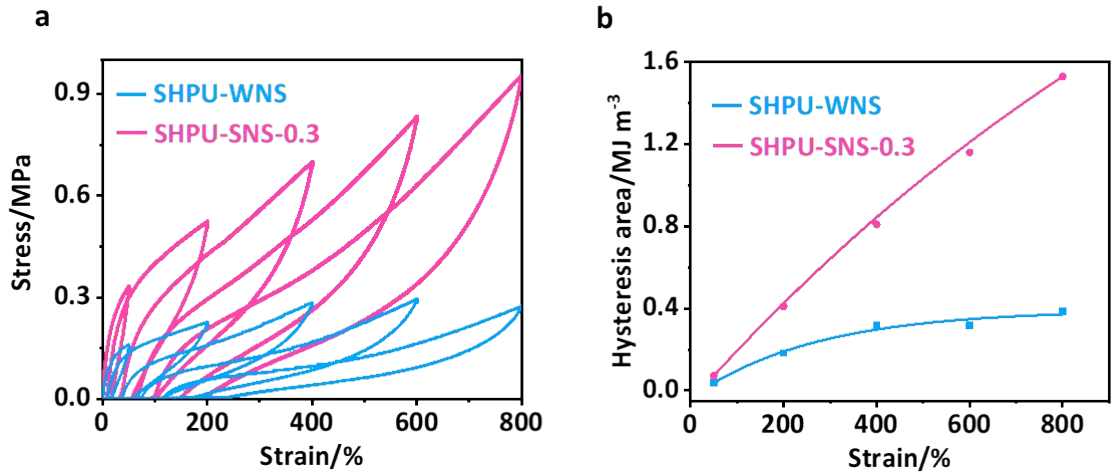

Fig. S13 a) Sequentially cyclic tensile tests of SHPU-SNS-0.3 SHPU-WNS from 50%, 200%, 400%, 600% to 800% without intervals. b) Hysteresis areas of SHPU-WNS and SHPU-SNS-0.3. Sequentially cyclic tensile test of SHPU-WNS and SHPU-SNS-0.3 was performed with gradually increased strains, where no waiting time between two consecutive loads (Fig. S13a). As shown in Fig. S13b, the hysteretic areas of SHPU-SNS-0.3 increased gradually in the five tensile cycles while the growth rate of hysteresis area slowed down significantly after the third tensile cycle for SHPU-WNS.

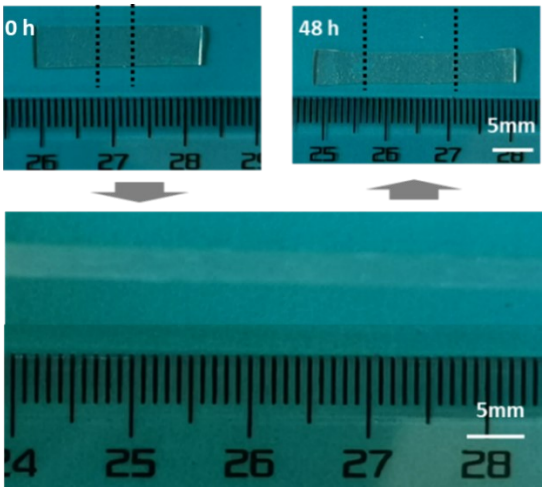

Fig. S14 Visual display demonstrating the poor elasticity of SHPU-WNS. When SHPU-WNS was stretched to a strain of 900%, it was unable to recover to its original length even after waiting for a long time of 48 h.

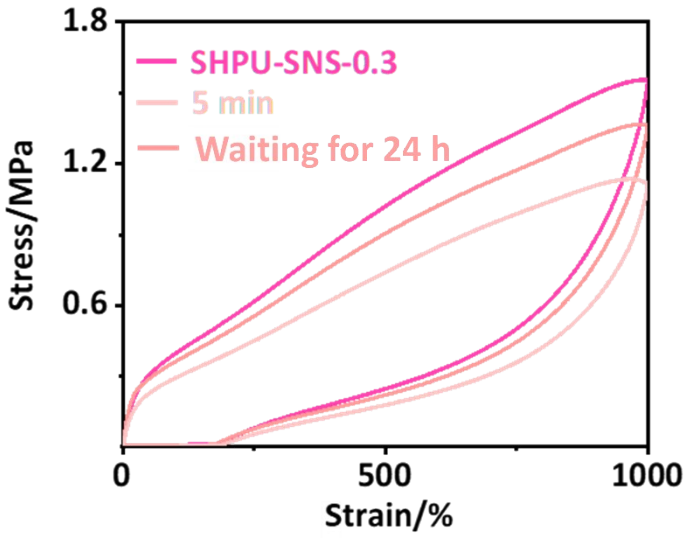

Fig. S15 Cyclic tensile curve of SHPU-SNS-0.3 with a large strain of 1000%. As shown, SHPU-SNS-0.3 could recover the residual strain in 5 min. However, after waiting for a long time of 24 h, the hysteresis loop was still not fully restored.

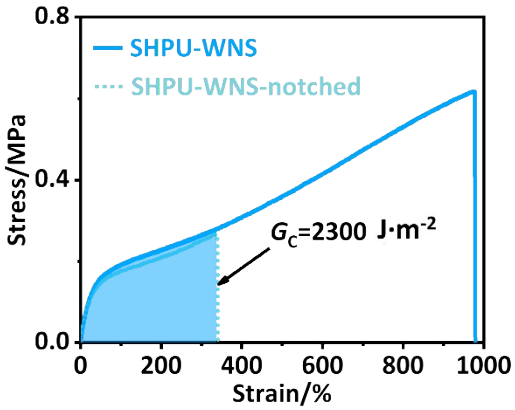

Fig. S16 Tensile curves of the intact and notched SHPU-SNS-0.3. As calculated, the SHPU-WNS had a relatively low fracture toughness of 2300 J·m^{-2}.

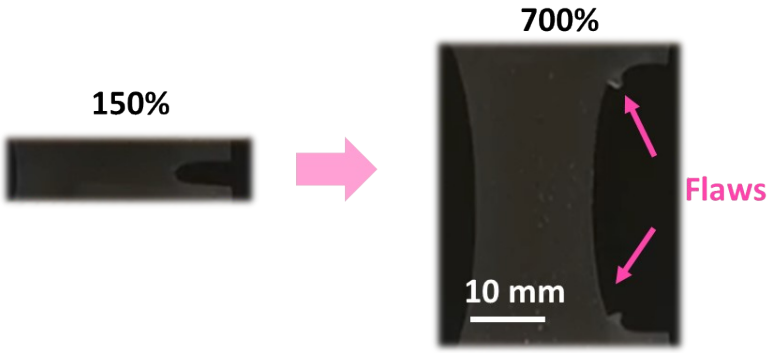

Fig. S17 Photographs of the notched region for SHPU-SNS-0.3 under the strains of 150% and 700%. There were obvious fiber-like flaws at both ends of the notched SHPU-SNS-0.3 sample at a strain of 700%.

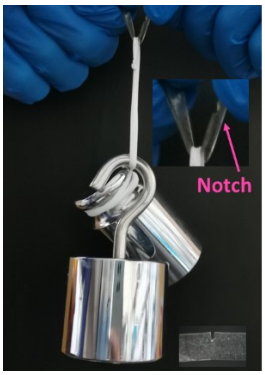

Fig. S18 Photographs of the load-bearing test of the pre-damaged SHPU-SNS-0.3 specimen. As shown, the pre-notched SHPU-SNS-0.3 specimen (0.5 g) could lift 2000 times its own weight (1 kg).

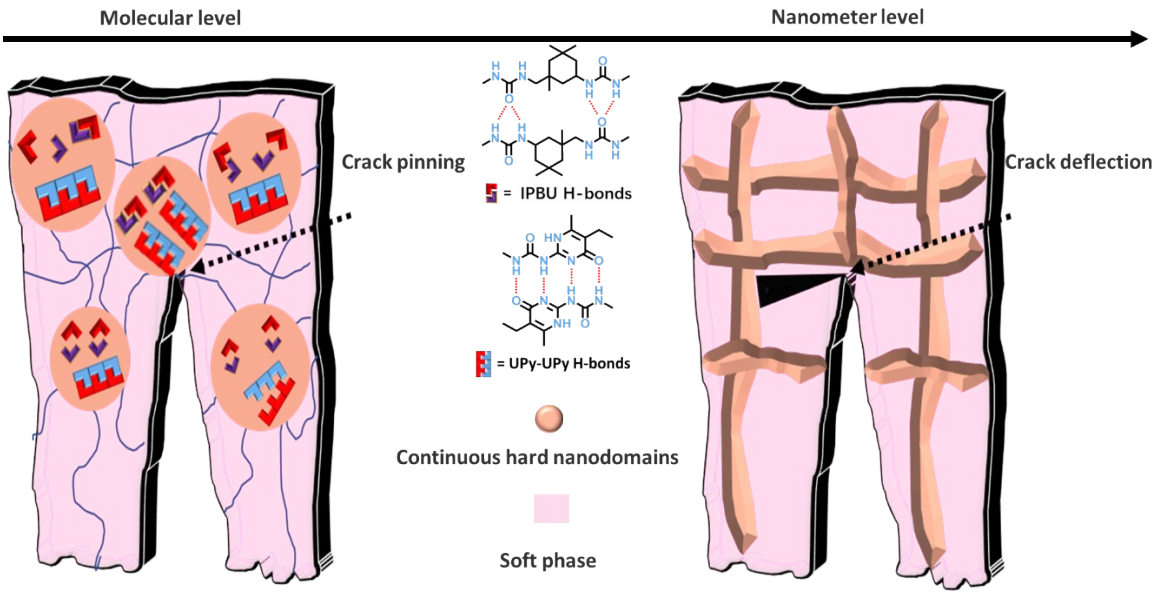

Fig. S19 Schematic illustration of mechanisms of resistance to crack propagation in SHPU-SNS-0.3. From a nanometer level, the continuous hard nanodomains acted as strong energy storage units to deflect the crack propagation. From a molecular level, the UPy motifs acted as robust and high-functionality crosslinkers, toughening the continuous hard nanodomains by virtue of their ability to delay the fracture of individual nanodomains by crack-pinning.

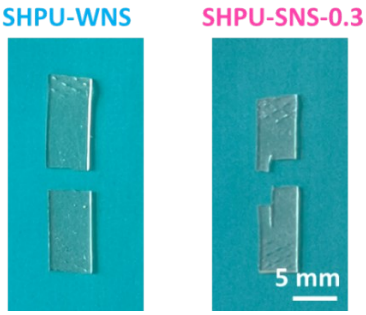

Fig. S20 The crack shapes of the fractured SHPU-WNS and SHPU-SNS-0.3 splines. For SHPU-WNS, the crack directly penetrated through the whole specimen. In sharp contrast, the crack propagated along the tensile direction of SHPU-SNS-0.3, and then passed through the whole specimen, demonstrating that the toughening effect caused by bicontinuous nanophase separation structure.

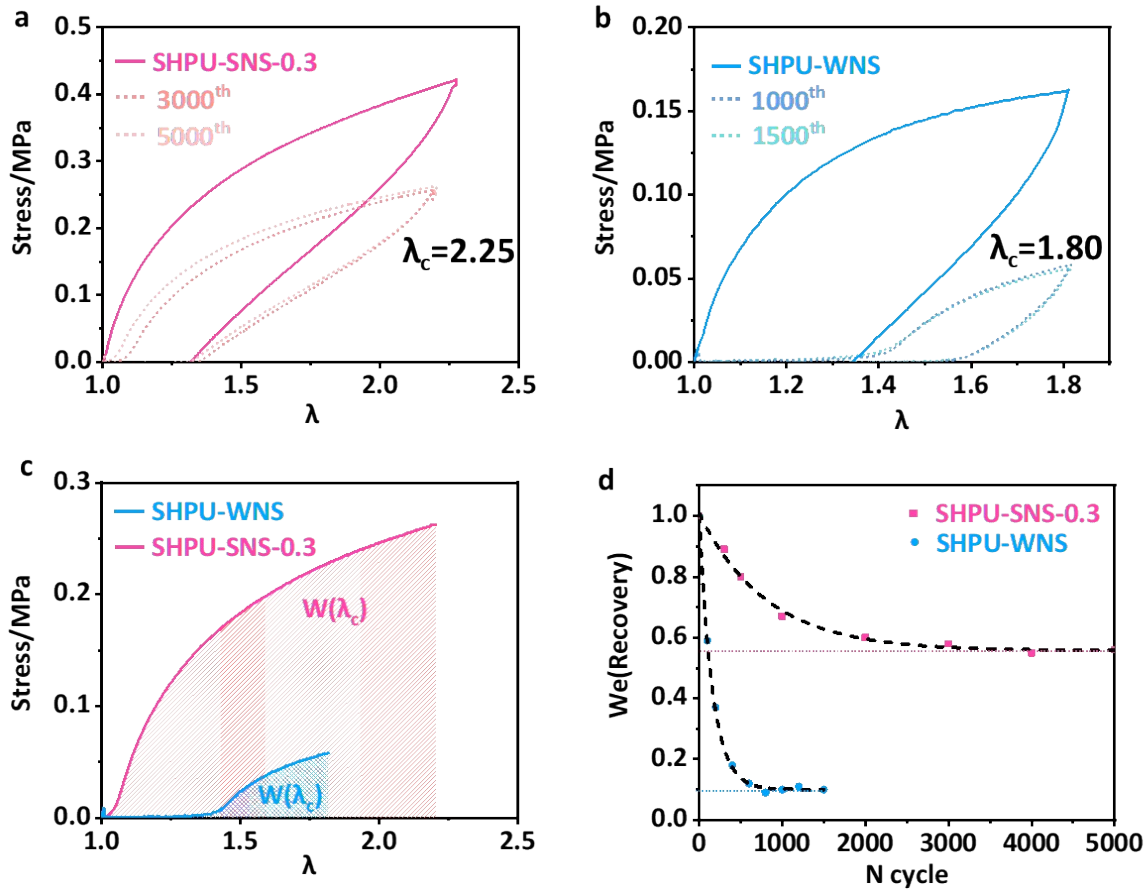

Fig. S21 The related curves of fatigue tests. a) Cyclic tensile curves of SHPU-SNS-0.3, which reached a steady state when N=3000 with a relaxation time of 12 h. b) Cyclic tensile curves of SHPU-WNS, which reached a steady state when N=800 with a relaxation time of 12 h. c) Stress-strain curves of SHPU-WNS, SHPU-SNS-0.3 after 1500, 5000 cycles, respectively. The W(λ_c) of SHPU-WNS was the strain energy density when λ_c=1.80 and the W(λ_c) of SHPU-SNS-0.3 was the strain energy density when λ_c=2.25. d) Recovery ratio of strain released energy of SHPU-WNS and SHPU-SNS-0.3 under different cycles. Taking SHPU-SNS-0.3 as an example, its hysteresis loop was gradually decreased with the increase of cycles, and eventually reached a steady state in 3000 cycles. After multiple cycles, the destructive supramolecular interactions and the slide of the chains could lead to the smaller and smaller hysteresis loop. As shown in Fig. S21a, after 12 h of relaxation, the sample could recover 57% of its original hysteresis. Hence, the traditional anti-fatigue mechanism of classical Lake-Thomas theory based on covalent network was no longer applicable to this system, and it should be replaced by a novel mechanism reported by Wang and co-workers. On this basis, the strain released energy of SHPU-SNS-0.3 was calculated to obtain the final fatigue threshold. As a result, the performance of SHPU-SNS-0.3 were better than those of SHPU-WNS in terms of critical strain, energy dissipation ability, and fatigue threshold, which meant that the bicontinuous network conspicuously improved the fatigue resistance.

Fig. S22 Photographs of pre-notched square SHPU-SNS-0.3 specimen after five and ten times of orthogonal tension.

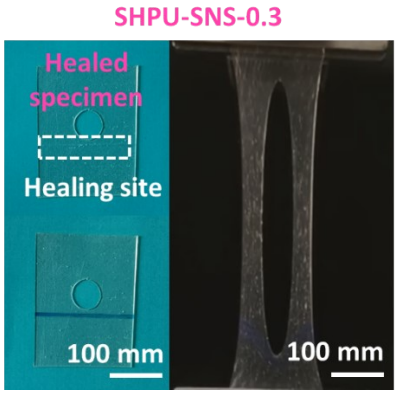

Fig. S23 Photographs of self-healed SHPU-SNS-0.3 specimen that could tolerate puncture and be stretched to 8 times its original length.

Fig. S24 Photographs of SHPU-SNS-0.3 reversibly stretched at 100 ˚C. As shown, SHPU-SNS-0.3 could be subjected to reversible large-strain stretching at high temperature, which indicated a high operating temperature for SHPU-SNS-0.3.

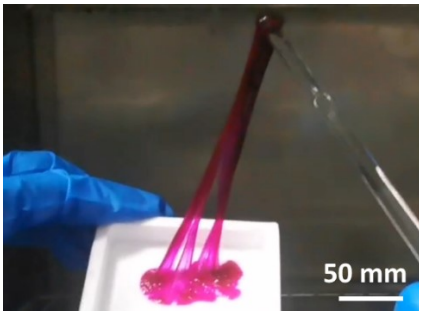

Fig. S25 Photographs demonstrating the flow state of SHPU-WNS at 100 ˚C. As shown, SHPU-WNS had adhered to the polytetrafluoroethylene mold at 100 ^{O}C, suggesting that it had lost the mechanical robustness.

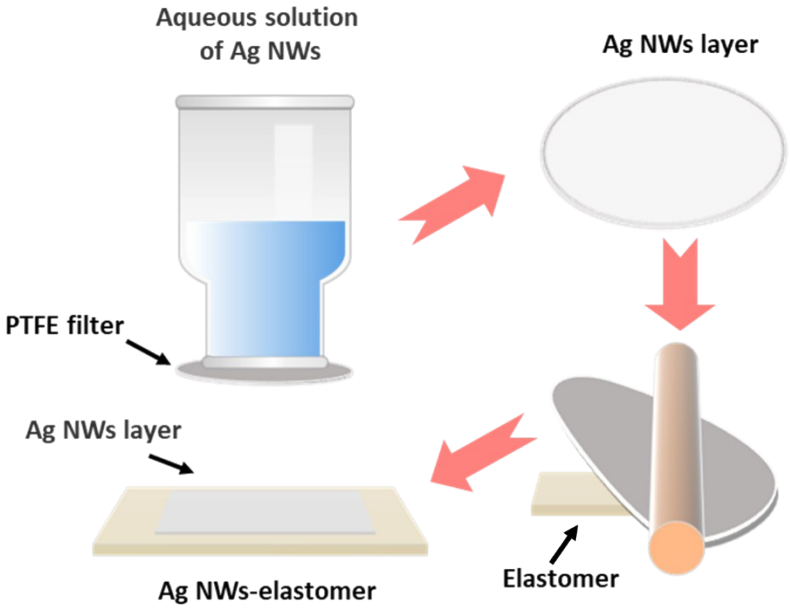

Fig. S26 The manufacturing process of Ag NWs/SHPU-SNS-0.3 strain sensor. Taking the elastomer as substrates, we attached the silver nanowires (Ag NWs) film obtained by suction filtration to the elastomer's surface for preparing a conductive strain sensor. Multiple hydrogen bonds inducing the strong interfacial adhesion made Ag NWs infiltrate into the elastomer. Thus, the Ag NWs could be kept in contact during the deformation of the substrate, maintaining the stability of fabricated strain sensor.

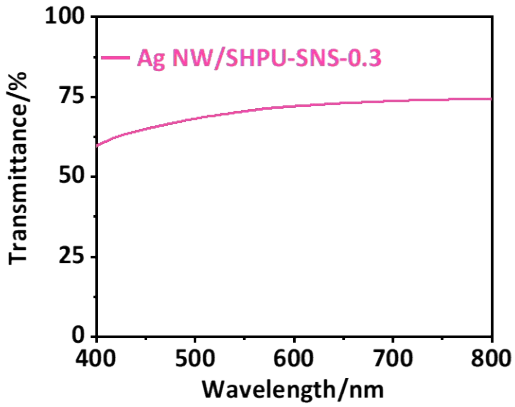

Fig. S27 Transmittance spectra of Ag NW/SHPU-SNS-0.3 strain sensor.

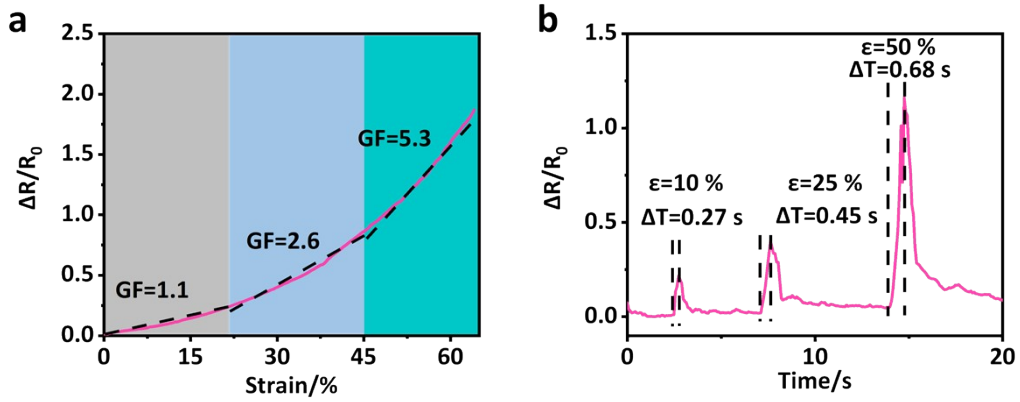

Fig. S28 a) Gauge factor (GF) of Ag NW/SHPU-SNS-0.3 strain sensor at various strains. b) Response time of Ag NW/SHPU-SNS-0.3 strain sensor at a strain of 10%, 25%, and 50%. As shown in Fig S28a, Ag NW/SHPU-SNS-0.3 strain sensor presented a wide sensing range of 64%. Fig. S28b indicated that Ag NW/SHPU-SNS-0.3 strain sensor exhibited different response time of 0.27 s, 0.45 s and 0.68s at various applied strain of 10 %, 25 %, and 50%, respectively.

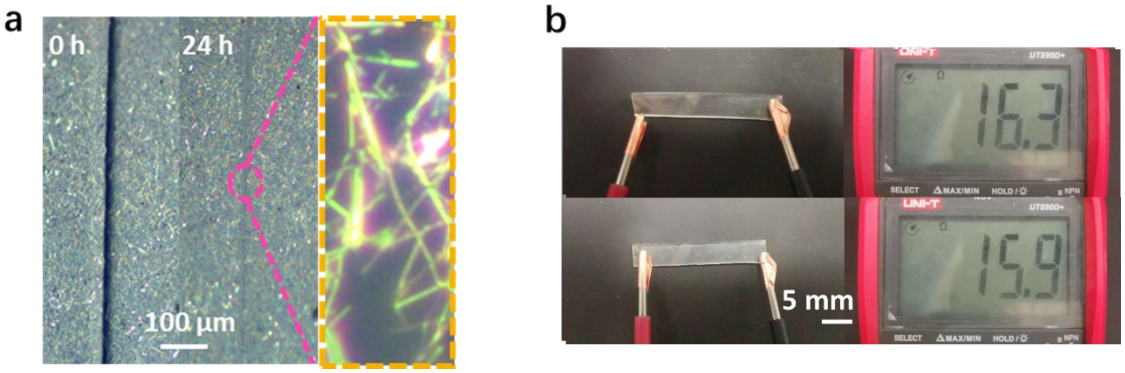

Fig. S29 a) Optical microscopic image of the scratched and healed Ag NWs/SHPU-SNS-0.3 strain sensor. b) Visual demonstrations of the restoration of conductivity. As shown in Fig. S29a, after waiting for 24 h, the percolated network structure could be spontaneously restored, and the re-spliced Ag NWs/SHPU-SNS-0.3 strain sensor could restore its conductivity (Fig. S29b).

2. Electronic Supplementary Tables

Table S1. Summary of mechanical properties of SHPU-WNS and SHPU-SNS-x

Sample	Stress/MPa	Strain/%	Young's modulus/MPa
SHPU-WNS	0.63±0.02	970±50	0.60±0.09
SHPU-SNS-0.1	0.95±0.09	1135±50	0.67±0.08
SHPU-SNS-0.3	2.60±0.11	1680±60	1.20±0.10
SHPU-SNS-0.5	3.40±0.11	1650±90	1.40±0.12

Table S2. Comparison of the elongation difference and stress difference of SHPU-SNS-0.3 with the reported soft materials

Sample	Elongation difference	Stress difference	Suppl. Ref.
Porous PDMS	1.06	3.71	2
PPG-PDMS-Zn	0.78	3.17	3
PDMS-TDI-AI	0.69	2.64	4
Si-A-IN10	0.96	2.06	5
PDMS-PUa-TFB	0.88	1.71	6
P3K5K-SS-IP	1.26	1.30	7
PBS/PDMS-1.5	0.68	0.67	8
PDMS-IPDI-TA	1.26	0.73	9
PIB-Eu-TTA0	1.98	0.89	10
U-PDMSK-E	1.76	0.20	11
SHPU-SNS-0.3	**1.65**	**4.2**	**Our work**

Table S3. Comparison of the elastic strain and recovery time of SHPU-SNS-0.3 with the reported self-recovery materials

Sample	Maximum applied strain/%	Fully recovered time/min	Suppl. Ref.
PU&=1/2	300	10	1
PA36,36	500	30	12
PDMS-MPU0.4-IU0.6	1000	30	13
PM-2	200	60	14
HM-PU2-SS	800	60	15
Cu-DOU-CPU	500	120	16
P2-Zn-0.5	100	240	17
PPGTD-IDA	300	360	18
PDM-2.5	1000	720	19
SHPU-SNS-0.3	**1000**	**5**	**Our work**

Table S4. Self-healing efficiency of SHPU-SNS-0.3 for different healing time at 25 °C

Healing time/h	Healed toughness/MJ m^{-3}	Healing efficiency/η
2	1.53	7%
24	6.99	31%
48	12.18	54%
72	22.40	99%

3. Electronic Supplementary Movies

Movie S1 This Movie showed that the crack in SHPU-SNS-0.3 was blunted and deflected along the tensile direction, while the cracks was directly penetrated in SHPU-WNS.

Movie S2 The Movie showed that the SHPU-SNS-0.3 spline could rebound spontaneously after being stretched at 100 °C.

Supplementary References

1. J. Li, H. Y. Niu, Y. F. Yu, Y. L. Gao, Q. Wu, F. F. Wang, P. C. Sun, *ACS Appl. Polym. Mater.,* 2021, **3**, 3373.

2. R. Woo, G. Chen, J. Y. Zhao, J. Bae, *ACS Appl. Polym*. *Mater*, 2021, **3**, 3496.

3. X. Z. Wu, R. Luo, Z. P. Li, J. Q. Wang, S. R. Yang, *Chem. Eng. J.,* 2020, **398**, 125593.

4. X. Z. Wu, J. Q. Wang, J. X. Huang, S. Y. Yang, *ACS Appl. Mater. Interfaces,* 2019, **11**, 7387.

5. F. B. Madsen, L. Y. Yu, A. L. Skov, *ACS Macro Lett.,* 2016, **5**, 1196.

6. Z. P. Yang, H. Q. Li, C. K. Li, X. J. Lai, X. R. Zeng, *Chem. Eng. J.,* 2022, **430**, 133103.

7. K. Y. Zhang, X. R. Shi, J. X. Chen, T. Xiong, B. Jiang, Y. D. Huang, *Chem. Eng. J.,* 2021, **412**, 128734.

8. P. Y. Qu, C. Lv, Y. H. Qi, L. Bai, J. P. Zheng, *ACS Appl. Mater. Interfaces,* 2021, **13**, 9043.

9. Z. P. Yang, H. Q. Li, L. Zhang, X. J. Lai, X. R. Zeng, *J. Colloid Interface Sci.,* 2020, **570**, 1.

10. J. Yang, D. Zhao, D. C. Yao, Y. G. Wang, H. R. Li, *Chem. Eng. J.,* 2021, **426**, 131595.

11. P. F. Cao, B. R. Li, T. Hong, J. Townsend, Z. Qiang, K. Y. Xing, K. D. Vogiatzis, Y. Y. Wang, J. W. Mays, A. P. Sokolov, T. Saito, *Adv. Funct. Mater.,* 2018, **28**, 1800741.

12. Y. Nurhamiyah, A. Amir, M. Finnegan, E. Themistou, M. Edirisinghe, B. Q. Chen, *ACS Appl. Mater. Interfaces,* 2021, **13**, 6720.

13. J. Kang, D. Son, G. N. Wang, Y. X. Liu, J. Lopez, Y. Kim, J. Y. Oh, T. Katsumata, J. Mun, Y. Lee, L. Jin, J. B. H. Tok, Z. Bao, *Adv. Mater.,* 2018, **30**, 1706846.

14. Z. Q. Zhou, S. Y. Chen, X. M. Xu, Y. Chen, L. P. Xu, Y. N. Zeng, F. Zhang, *Prog. Org. Coat.,* 2021, **154**, 106213.

15. J. C. Ma, S. F. Wen, Z. Y. Zhou, *Langmuir,* 2022, **38**, 8862.

16. L. Z. Zhang, Z. H. Liu, X. L. Wu, Q. B. Guan, S. Chen, L. J. Sun, F. Y, S. L. W. Guo, J. C. Song, E. M. Jeffries, C. L. He, F. L. Qing, X. G. Bao, Z. W. You, *Adv. Mater.,* 2019, **31**, 1901402.

17. P. J. Zhao, L. L. Wang, L. F. Xie, W. Y. Wang, L. L. Wang, C. Q. Zhang, L. Li, S. Y. Feng, Macromol. *Rapid Commun.,* 2021, **42**, 2100519.

18. D. Wang, J. H. Xu, J. Y. Chen, P. Hu, Y. Wang, W. Jiang, J. J. Fu, *Adv. Funct. Mater.,* 2020, **30**, 14.

19. Y. H. Li, W. J. Li, A. L. Sun, M. F. Jing, X. J. Liu, L. H. Wei, K. Wu, Q. Fu, *Mater. Horiz.,* 2021, **8**, 267.